Enhanced Photocatalytic Activity of Heterostructured Ferroelectric $BaTiO_3$/α-Fe_2O_3 and the Significance of Interface Morphology Control

Yongfei Cui,[†‡] *Joe Briscoe,*[‡] *Yaqiong Wang,*[‡] *Nadezda V. Tarakina,*[‡] *Steve Dunn*[*‡]

† School of Materials Science and Engineering, Shaanxi University of Science and Technology

Xi'an 710021, Shaanxi, P. R. China

‡ Materials Research Institute, School of Engineering and Materials Science, Queen Mary University of London, Mile End Road, London E1 4NS, U. K.

KEYWORDS: Ferroelectric, Barium Titanate, Heterostructure, Photocatalysis, Interface Morphology

ABSTRACT: We have used a ferroelectric $BaTiO_3$ substrate with a hematite (α-Fe_2O_3) nanostructured surface to form a heterogeneous $BaTiO_3$/α-Fe_2O_3 photocatalyst. In this study we show that differing the mass ratios of α-Fe_2O_3 on the $BaTiO_3$ has a significant influence on photoinduced decolourisation of Rhodamine B under simulated sunlight. The highest photocatalytic activity was obtained for $BaTiO_3$-Fe_2O_3-0.001M relating to the lowest mass ratio of α-Fe_2O_3 in our study. This catalyst exhibited a two-fold increase in performance compared to

pure $BaTiO_3$ and a five-fold increase when compared to the higher surface area pure α-Fe_2O_3. The increases in performance become more marked when scaled for the lower surface area of the heterostructured catalyst. The performance enhancement is associated with improved charge carrier separation at the interface between the ferroelectric surface, which exhibits a ferroelectric polarization, and the hematite. Increasing the mass ratio of hematite increases the thickness of this layer, lowers the number of triple-point locations, and results in reduced performance enhancement. We show that the reduced performance is due to a lack of light penetrating into $BaTiO_3$ and the relationships between the depolarization field from the ferroelectric and carriers in the hematite. Our findings demonstrate that it is possible to use the built-in electric field of a ferroelectric material to promote charge carrier separation and boost photocatalytic efficiency.

Introduction

For some years semiconductor photocatalysis has been part of the toolbox of strategies to address environmental remediation such as wastewater treatment and indoor air purification, [1,2] and facilitate solar fuel production. There are still inherent problems such as low carrier diffusion lengths and internal recombination of carriers that prevent a meaningful penetration of semiconductor photocatalysts into commercial applications.[3] An efficient photocatalyst must fulfill defined criteria that include an appropriate band gap and band-gap configuration, effective charge carrier separation and chemical stability.[4] It is being recognised that there are few, if any, single material systems that satisfy all these requirements simultaneously. The search is now on for combinations of materials that produce heterojunctions to improve photocatalytic efficiency by manipulation of interfacial charge transfer and separation and enhancement of visible-light-

harvesting.[5–7] The advantage of heterojunctions between semiconductors for photocatalytic applications has been subject of review articles.[8,9]

Due to the existence of spontaneous polarization in ferroelectric materials, photogenerated electrons and holes in the space charge layer can be spatially separated and migrate in opposite directions.[10–12] The internal-field-driven separation of electrons and holes inhibits recombination of charge carriers and increases their lifetime.[13] These unique properties make ferroelectric materials promising candidates for effective photocatalysts, and a series of ferroelectric materials such as $LiNbO_3$, $BaTiO_3$ have been successfully applied in semiconductor photocatalysis.[14,15]

The benefits of using a ferroelectric material also extend to the manner in which the material screens the surface charge. It was demonstrated that the H_2 generation rate of a thin TiO_2 film deposited on poled single crystal of $LiNbO_3$ was dependent on the polarization conditions.[16] In addition, Rohrer et al. demonstrated that the spatially separation of redox reactions also happened on a thin layer of TiO_2 on ferroelectric $BaTiO_3$ substrates.[17] All these phenomena were ascribed to the external screening of the surface charge in ferroelectrics arising from ferroelectric polarization, and the dipoles in ferroelectric substrates are expecting to impact on the motion of charge carriers in the semiconductor thin films on top. Considering these intriguing polarization-dependent surface properties, a series of these heterogeneous photocatalysts composed of ferroelectrics and nonferroelectric semiconductors have been developed, including $BiFeO_3/TiO_2$,[18,19] PZT/TiO_2,[20] $PbTiO_3/TiO_2$,[21] etc. The enhanced photocatalytic activity of these composite-structured photocatalysts was ascribed to the charge carriers separation promoted by the ferroelectric polarization and/or the heterojunction structure, and the enhanced surface area of the nanostructured shell.

Hematite (α-Fe_2O_3) has been widely applied in photoelectrocatalytic water splitting,[22] enviromental remediation,[2] etc. due to its favorable optial band gap (1.9 ~2.2 eV),[23] abundance, good stability, non-toxicity, and low cost. However, it suffers from very short hole diffusion length and charge carrier lifetime.[24] Considering the drawbacks of α-Fe_2O_3, we attempted to combine a ferroelectric material with α-Fe_2O_3, and expected that the ferroelectric dipole and heterojunction can endow the heterostructured photocatalyst with an excellent photoactivity. To our knowledge there are few reports of heterostructured photocatalysts combining α-Fe_2O_3 and ferroelectric semiconductors. In this study, we choose ferroelectric $BaTiO_3$, which has been shown to be a promising candidate for photocatalysis,[15] as the other component to form a heterojunction with α-Fe_2O_3 and investigate the photocatalytic activity of the heteostructured photocatalyst $BaTiO_3$/α-Fe_2O_3 in photodecolourisation of organic dye under simulated solar light.

Experimental Methods

$BaTiO_3$ was supplied by Sigma (99.9% trace metal basis, <2 μm) and post-processed to produce a ferroelectric powder.[15] The heterostructured $BaTiO_3$/α-Fe_2O_3 catalysts were prepared by dissolving the required amount of $Fe(NO_3)_3 \cdot 9H_2O$ in 30 ml ethanol to obtain a concentration (Fe^{3+}) of 0.001M, 0.01M, 0.1M and 0.5M. 1.5 g of $BaTiO_3$ was added to the ethanol solution and vigorously stirred at room temperature for 30 minutes. This was followed by ultra-sonication for 30 minutes and evaporation of the ethanol at 50 ºC. The powder was then annealed at 300 ºC for 10 minutes followed by thorough ethanol-washing. The powder was finally annealed at 300 ºC for 6 hours. The as-prepared powders were termed BTO-Fe_2O_3-0.001M, BTO-Fe_2O_3-0.01M, BTO-Fe_2O_3-0.1M and BTO-Fe_2O_3-0.5M according to the iron nitrate concentration used. For control, α-Fe_2O_3 was prepared using the same method without adding BTO as a support.

The phase compositions of the powders were analysed using X-ray diffractometer (Panalytical Xpert Pro diffractometer) with Cu-K_α radiation. The morphology of the powders was observed using SEM (scanning electron microscopy, FEI Inspect F) and TEM (transmission electron microscopy, Jeol JEM 2010). The BET (Brunauer-Emmett-Teller) surface area of all samples was obtained on surface area analyser (Micromeritics Gemini VII). The surface chemical composition of the powders was detected by XPS (X-ray photoelectron spectroscopy, Thermo Scientific K-Alpha) with an Al Kα source (1486 eV), and the binding energies of all peaks were corrected to C 1s (284.9 eV). Photoluminescene spectra were obtained using fluorescene spectrophotometer (Edinburgh FS5) equipped with a 150 W Xenon lamp and the excitation wavelength was 315 nm.

The photocatalytic performance of the catalysts was assessed by photodecolourisation of Rhodamine B dye solution under simulated sunlight. 50 ml RhB dye solution (10 ppm) was mixed with 0.15 g photocatalyst powder, followed by vigorous stirring for 30 minutes in dark to achieve an adsorption-desorption equilibrium. Then the solution was exposed under simulated sunlight with an irradiation intensity of 100 $mWcm^{-2}$. During the photodecolourisation process, about 2 ml of the solution was sampled every 30 minutes, followed by centrifugation. Then the concentration of the dye solutions was analysed using UV-Vis spectrophotometer (Perkin Elmer Lambda 950). The transient photocurrent was measured on a CHI660E electrochemical station (Shanghai Chenhua, China) using Na_2SO_4 (0.5 M, pH 6.5) solution as the electrolyte, Ag/AgCl as the reference electrode and a Pt sheet as the counter electrode. The powdered photocatalysts were deposited onto FTO which was employed as the working electrode. A 300 W xenon lamp was used as the light resource and a distance of 10 cm was fixed between the lamp and the working electrode.

Results and Discussion

Characterisation of catalyst structures

The morphologies of the photocatalysts were observed using SEM, shown in Figure 1. The morphologies of BTO-Fe_2O_3-0.001M particles (Figure 1a) are very similar in appearance to the control pure $BaTiO_3$ (Figure S1). Increasing the amount α-Fe_2O_3 adds extra features to the surface of the $BaTiO_3$. The most significant observation is an increase in texture on the $BaTiO_3$ with a secondary phase being distributed on the surface. The new feature is clearly shown in Figure 1c and (d). EDS analysis (Figure 1f) confirms the existence of Fe and demonstrates that iron species have been deposited on the surface. The morphology of α-Fe_2O_3 is also shown in Figure 1e.

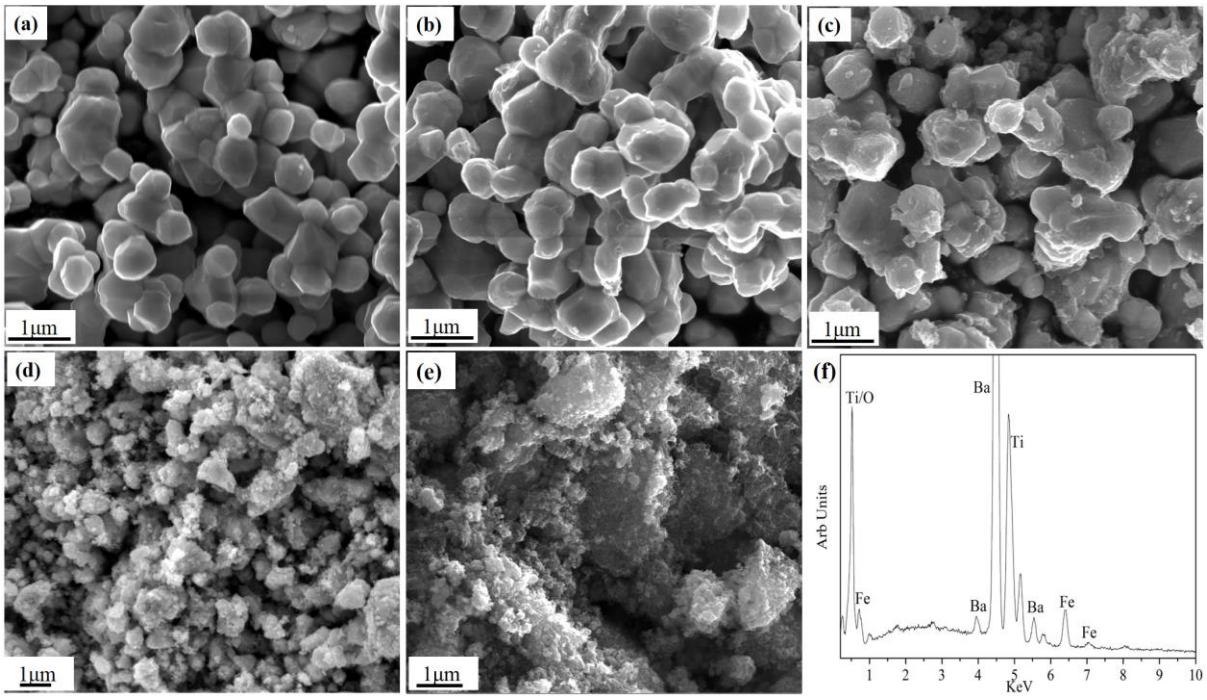

Figure 1. SEM micrographs of (a) BTO-Fe_2O_3-0.001M, (b) BTO-Fe_2O_3-0.01M, (c) BTO-Fe_2O_3-0.1M, (d) BTO-Fe_2O_3-0.5M, (e) Fe_2O_3 and (f) EDX spectrum of BTO-Fe_2O_3-0.01M. With increasing of Fe_2O_3 mass ratio, the surface morphologies of the photocatalysts change and a secondary species can be seen on the surface. The EDX spectrum shows the existence of Fe species on the surface.

The phase compositions of the prepared catalysts were analysed using X-Ray diffraction and the associated patterns are shown in Figure 2. We are able to index the diffraction peaks of synthesised Fe compound to hematite (α-Fe_2O_3 (JCPDS33-0664)). We note that in the XRD patterns of the heterostructured BTO-Fe_2O_3 photocatalysts the characteristic patterns of α-Fe_2O_3 are absent for BTO-Fe_2O_3-0.001M, 0.01M and 0.1M. In these cases it is only possible to assign tetragonal $BaTiO_3$ (JCPDS 05-0626) peaks. With further increased loading of Fe_2O_3, BTO-Fe_2O_3-0.5M, the characteristic peaks of both α-Fe_2O_3 and $BaTiO_3$ are present (see Figure 2d). This can be explained by the extremely small quantity of Fe_2O_3 in all heterostructured catalysts except for BTO-Fe_2O_3-0.5M, as seen in SEM and TEM (below) analysis. Such low interaction

cross sections mean that it is not possible to obtain an X-ray diffraction pattern under our experimental conditions. A similar phenomenon has been previously reported.[25]

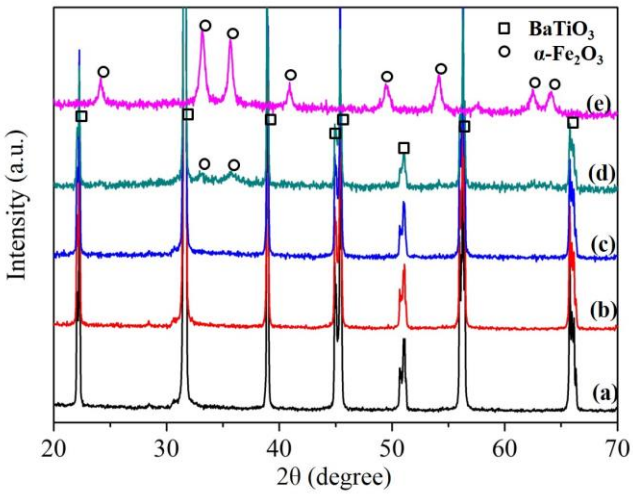

Figure 2. XRD patterns of $BaTiO_3/Fe_2O_3$ (a to d) and pure α-Fe_2O_3 (e). (a) to (d) represents BTO-Fe_2O_3-0.001M, BTO-Fe_2O_3-0.01M, BTO-Fe_2O_3-0.1M and BTO-Fe_2O_3-0.5M. The characteristic peaks of BTO and α-Fe_2O_3 overlap in the synthesised heterostrutured BTO-Fe_2O_3-0.5M.

A comparison of XPS spectra between the $BaTiO_3$ substrate and BTO-Fe_2O_3-0.001M are presented in Figure 3a. The XPS peaks of elements Ba, Ti and O of these two samples overlap, as shown in Figure S2, and no significant discrepancy was observed. Extra signals from Fe are seen in the BTO-Fe_2O_3-0.001M sample. As indicated in Fig. 3b, the spectrum of Fe 2p in BTO-Fe_2O_3-0.001M is made up of two characteristic peaks, Fe $2p_{1/2}$ at 724.2 eV and $2p_{3/2}$ at 710.7 eV. As for the peak positions of Fe $2p_{3/2}$ in α-Fe_2O_3, many different values have been reported, which normally range from 710.6 to 711.2 eV.[24,26,27] The results obtained in this work are consistent with the reported data, indicating the chemical valence of Fe^{3+} in the as-prepared sample. In addition, the peak fittings clearly showed a peak at ~ 718.7 eV between Fe $2p_{1/2}$ and

Fe $2p_{3/2}$ peak. This peak is considered as the associate satellite peak of Fe $2p_{3/2}$ main peak, which is a characteristic feature of Fe^{3+} in α-Fe_2O_3.[24,26,27] Overall, the analysis of the XPS spectra supports the formation of α-Fe_2O_3 on the surface of heterostructured BTO-Fe_2O_3 photocatalysts.

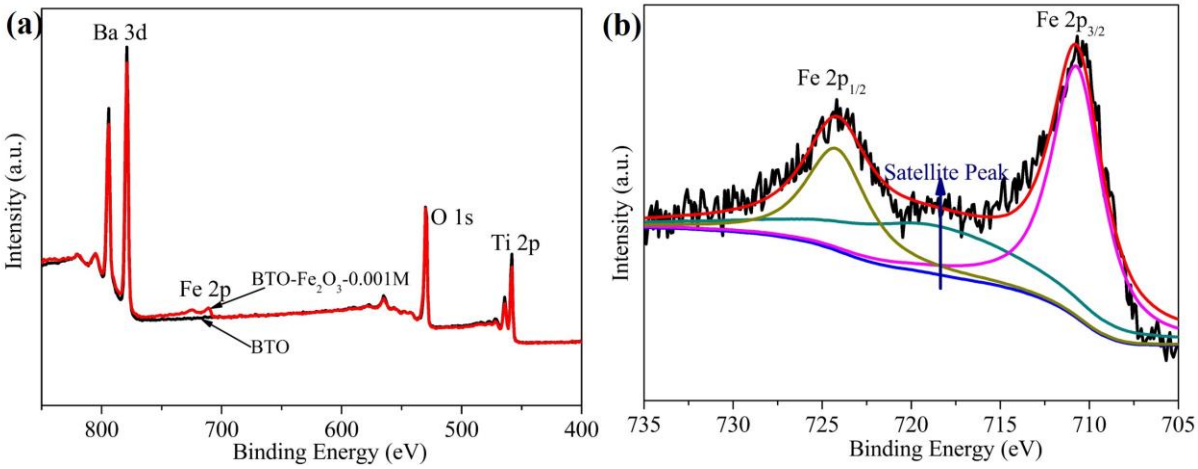

Figure 3. (a) XPS spectra of BTO and BTO-Fe_2O_3-0.001M. (b) XPS spectrum of Fe 2p in BTO-Fe_2O_3-0.001M. Compared to BTO, additional Fe 2p spectrum can be observed in BTO-Fe_2O_3-0.001M sample. The characteristic XPS spectrum of Fe 2p in α-Fe_2O_3 confirms the existence of α-Fe_2O_3 on the surface of BTO-Fe_2O_3-0.001M.

The microstructures of BTO-Fe_2O_3 systems were further investigated by TEM (Figure 4). In contrast to the smooth edge of plain $BaTiO_3$ (see Fig. S3a), some secondary-phase nanoparticles with an average size below 10 nm formed on the surface of $BaTiO_3$ particles in BTO-Fe_2O_3-0.001M, as seen Fig. 4a. With an increase in $Fe(NO_3)_3$ concentration during synthesis, the thickness of the Fe containing layer increased and gave a maximum average for BTO-Fe_2O_3-0.5M at 84 nm, shown in Figure S3c. It should be noted that the thickness of the secondary-phase layer is not uniform and varies for the samples with high loading quantity, as would be expected for the agglomeration of secondary particles on a primary substrate. The thickness of this layer was measured choosing different areas and particles, and then averaged. In addition, an

elemental map was obtained for this layer (Figure 4c-f), which shows Fe distributed around the outside of the particle, where Ba and Ti were detected in the core of the particle. When consideration is given to the analytical data generated – XRD, XPS and SEM/EDS results – we have clear evidence to show that the secondary phase around the $BaTiO_3$ core is α-Fe_2O_3. In addition, the TEM micrographs demonstrate that an intimate junction between $BaTiO_3$ and α-Fe_2O_3 was formed during synthesis. Based on the morphology changes of α-Fe_2O_3 on the surface of BTO observed in TEM micrographs, it can be concluded that the interface morphology of heterostructured photocatalysts can be manipulated through adjusting the concentration of Fe^{3+} precursor, evolving from island-like nanoparticles to a thick layer of α-Fe_2O_3. This interface morphology evolution can have a potential impact on the photocatalytic properties, which will be further discussed in detail.

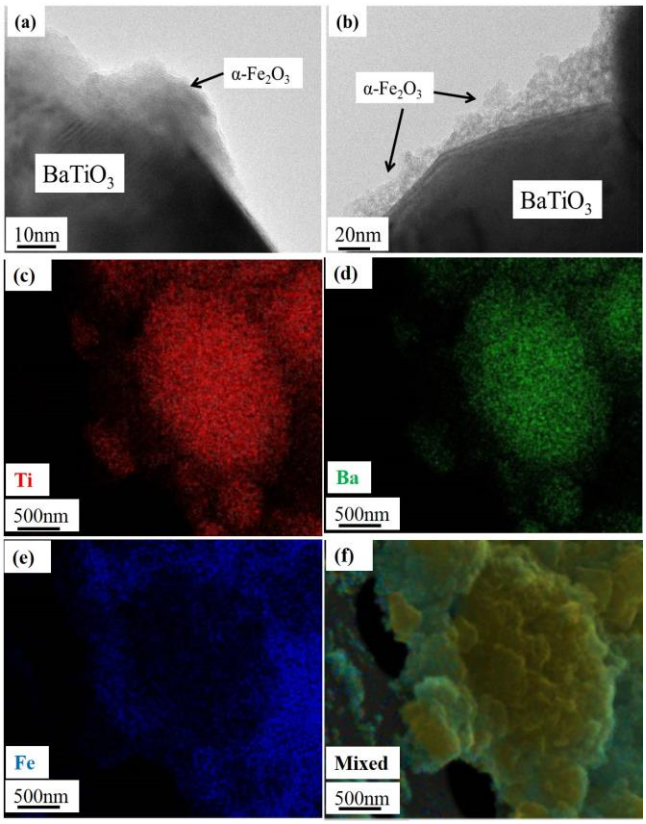

Figure 4. TEM micrographs of (a) BTO-Fe_2O_3-0.001M, (b) BTO-Fe_2O_3-0.01M and EDS mapping of BTO-Fe_2O_3-0.5M (c)-(f). The conjunction between BTO and Fe_2O_3 is observed.

The optical properties of the photocatalysts were investigated using UV-Vis diffuse reflectance spectroscopy and the spectra are shown in Figure 5a. Meanwhile the bandgaps of the samples were estimated based on the Tauc plot of $(\alpha h\upsilon)^2$ vs. $h\upsilon$ according to the equation: $(\alpha h\upsilon)^n = A(h\upsilon - E_g)$, where α, A, υ and E_g represent the absorption coefficient, proportionality, light frequency and bandgap respectively. As presented in Figure 5b, the bandgaps of BTO, BTO-Fe_2O_3-0.001M, BTO-Fe_2O_3-0.01M, BTO-Fe_2O_3-0.1M, BTO-Fe_2O_3-0.001M-0.5M and Fe_2O_3 are estimated to be 3.14 eV, 3.1 eV, 3.0 eV, 2.72 eV, 1.89 eV, 1.88 eV respectively. According to Fig. 5a, the absorption intensity of the heterostructured system increases in the visible-light range when compared with pure BTO. This is due to the coating of Fe_2O_3, which has a narrow band gap (ca. 1.88 eV) and can absorb light in the visible-light range. Furthermore,

this visible absorption increases with increasing Fe_2O_3 quantity. There is a distinct shape change of the absorption spectra that can be observed upon addition of Fe_2O_3, with a clear absorption onset around 400 nm in the pure BTO catalyst and in samples with a low mass ratio of Fe_2O_3 (BTO-Fe_2O_3-0.001M and BTO-Fe_2O_3-0.01M). This is related to the major absorption by the core BTO in these samples, which can be supported by the estimated bandgap values in Fig. 5b, i.e. the bandgaps of BTO-Fe_2O_3-0.001M and BTO-Fe_2O_3-0.01M are close to that of BTO. In contrast, this absorption onset assigned to BTO was not observed in the systems with higher Fe_2O_3 content and the absorption spectra were similar to pure Fe_2O_3. This indicates that the main photon-absorption species change from the BTO core to the Fe_2O_3 shell with increasing quantity of surface loaded Fe_2O_3. Accordingly, the bandgaps of the samples with high Fe_2O_3 content are more close to that of pure Fe_2O_3 other than BTO (Fig. 5b).

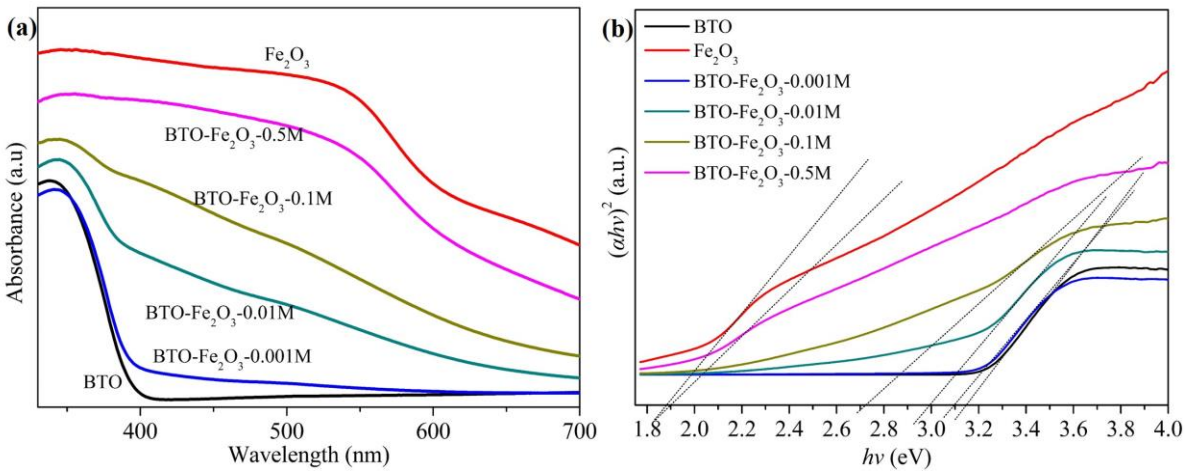

Figure 5. (a) Diffuse reflectance spectra of heterostructured BTO-Fe_2O_3, BTO and Fe_2O_3. (b) Plots of $(\alpha h\upsilon)^2$ vs. $h\upsilon$ of samples. With the increasing loading of Fe_2O_3, an absorption enhancement in visible-light range is observed and the bandgaps of samples become narrower, indicating a shift of photon-absorption center from BTO to Fe_2O_3.

Assessment of photocatalytic activity

The dye-molecule adsorption results are listed in Table S1. After adsorption-desorption equilibrium in dark, the largest adsorption was observed in α-Fe_2O_3 which has the largest surface area. Bare BTO and BTO-Fe_2O_3-0.001M showed similar adsorption amount, but smaller compared with α-Fe_2O_3. The photocatalytic activity of these photocatalysts was measured by photodecolourisation of Rhodamine B under simulated solar light. Figure 6 shows the degradation profiles of the photocatalysts tested.

The kinetics of photodecolourisation of RhB using the synthesised photocatalysts follows the zero-order rate law,[28,29] shown in Figure 6a, which can be expressed as follows:

$$C_0 - C_t = kt \quad (1)$$

Where C_0 is the initial concentration of the dye solution, C_t the concentration of the dye solution after irradiation for the time t, and the reaction rate k .The reaction rate k can be obtained from the slope of $C_0 - C_t$ vs. t (See Figure S4 in the Supporting information) with the results being presented in Figure 6b.

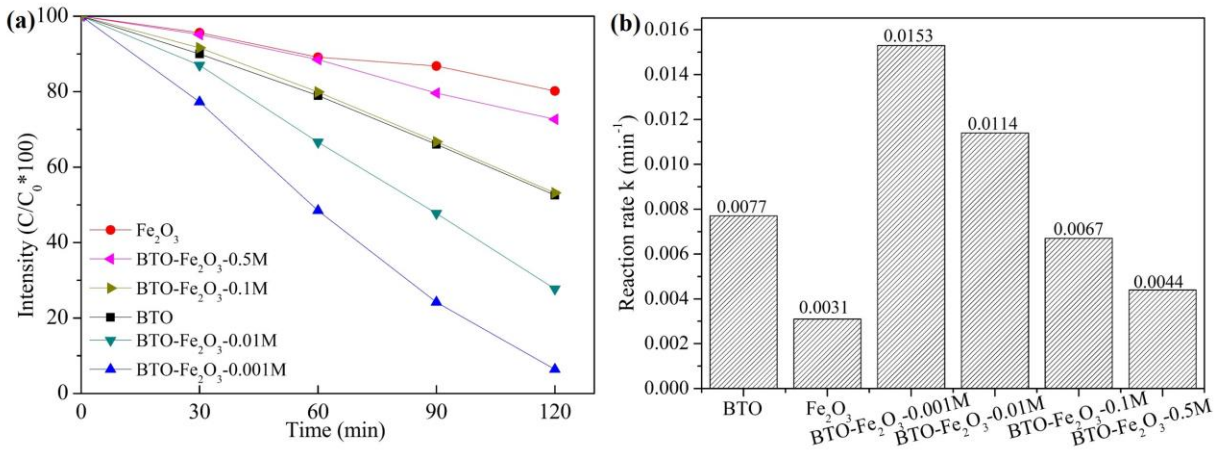

Figure 6. (a) Photodecolourisation profiles of RhB with different photocatalysts under simulated sunlight. Heterostructured BTO-Fe_2O_3-0.001M shows the best photocatalytic activity. (b) The calculated reaction rates of different photocatalysts. BTO- Fe_2O_3-0.001M and BTO- Fe_2O_3-0.01M show faster reaction rates than their single components.

Comparing the reaction rates obtained for different samples, two main effects can be observed. Firstly, after combining $BaTiO_3$ with Fe_2O_3, the heterostructured photocatalysts (BTO-Fe_2O_3-0.001M and BTO-Fe_2O_3-0.01M) showed improved photocatalytic activity when compared to either $BaTiO_3$ or Fe_2O_3. The maximum reaction rate was obtained for BTO-Fe_2O_3-0.001M which demonstrates two-fold enhancement over $BaTiO_3$ and five-fold enhancement over Fe_2O_3 despite of a minimum RhB adsorption on BTO-Fe_2O_3-0.001M. Secondly it was also observed that the enhancement in photocatalytic activity decreased with increased Fe_2O_3 coating. For BTO-Fe_2O_3-0.5M where the mass percentage of Fe_2O_3 is about 44%, the photodecolourisation rate is close to that of pure Fe_2O_3.

Radical Trapping Experiment

In order to uncover the mechanisms of photodegradation, the reactive radicals during photodegradation were detected through the addition of various radical scavengers. EDTA was selected as a hole scavenger and ethanol was chose as a hydroxyl radical scavenger.[30] As shown in Fig. 7, with the addition of ethanol, the overall degradation was inhibited to some extent. About 70% of RhB molecules were degraded in comparison with almost 100% degradation when no scavenger was added. When adding EDTA to the dye solution, the degradation process was significantly restrained and minor degradation was observed. Considering the role of hole scavenger of EDTA, it is believed that the inhibition of photocatalytic reactions is related to the quench of holes by EDTA. Overall, the radical trapping experiments demonstrated that holes are playing a dominate role in the degradation process.

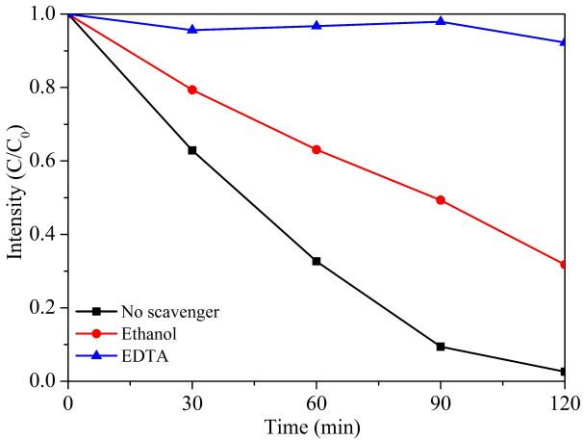

Figure 7. Comparison of degradation profiles with BTO-Fe_2O_3-0.001M with or without adding ethanol and EDTA. A significant inhibition of degradation after the addition of EDTA suggested holes were the main reactive radicals during the degradation.

Recyclability Test

The stability of the photocatalysts were tested as well and the results are shown in Figure 8a. No significant deterioration in photocatalytic activity of BTO-Fe_2O_3-0.001M was observed. The minor change in the XRD pattern of BTO-Fe_2O_3-0.001M after recycle test implies a good stability of the photocatalyst. (Figure 8b)

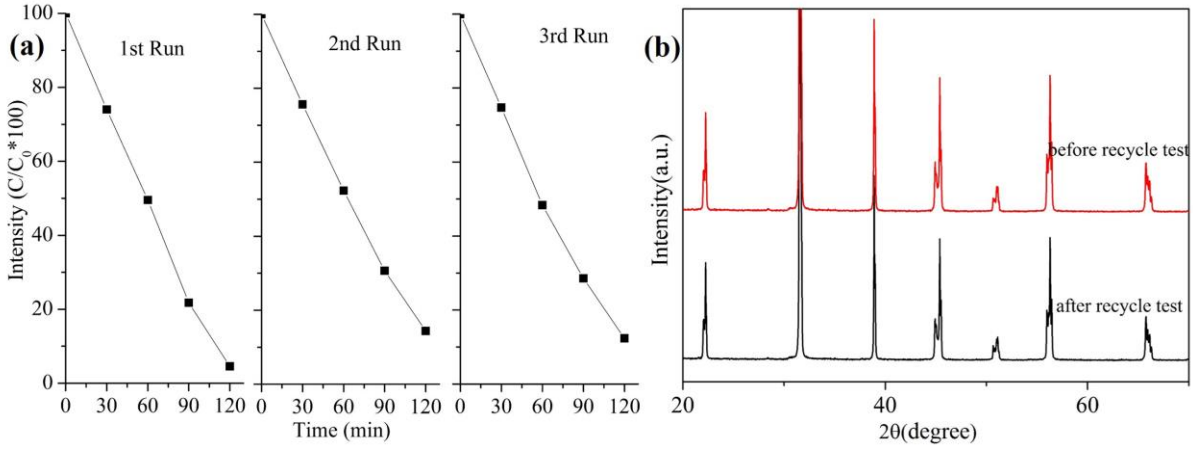

Figure 8. (a) Photodecolourisation profiles of RhB using heterostructured BTO-Fe_2O_3-0.001M under solar simulator in the recycling reactions. The minor change in the decolourisation percentage after three recycles indicates a good photocatatytic stability. (b) The XRD patterns of BTO-Fe_2O_3-0.001M before and after recycle test. Minor changes were observed, indicating a good stability of photocatalysts.

Discussions

Normally the morphologies, surface areas, light absorption and band gap configurations of a photocatalyst are impacting its performance. To determine which of these elements plays the major role in the observed rate enhancement in our work, these factors will be discussed one by one. The TEM images show some very clear changes to the catalysts surfaces and this is also associated with changes in the surface area (Table S1). The BET surface areas of the catalysts

increase from below 1 m^2/g for BTO-Fe_2O_3-0.001M to over 23 m^2/g for BTO-Fe_2O_3-0.1M. Large surface areas are generally considered beneficial as they provide more active sites for reactions on the surface. In order to exclude the effect of surface area on the photochemical processes the reaction rates of different photocatalysts were normalized by surface area, shown in Figure S5. After excluding the influence of surface area, the fastest reaction rate was obtained the Fe_2O_3-0.001M system which was 2.5 times faster than for pure $BaTiO_3$ and over 500 times faster than Fe_2O_3 control catalyst. Indeed, it is somewhat surprising that highest photocatalytic activity was obtained for BTO-Fe_2O_3-0.001M, which had the smallest surface area for all heterostructured catalysts. Our observed trend of photocatalytic rate vs. surface area indicates that surface area is not the main factor contributing to the higher photoreaction rate.

Another influencing factor may be the improved visible-light harvesting. In order to confirm this, the photocatalytic performance with BTO-Fe_2O_3-0.001M and bare BTO was compared under visible light with the UV portion removed by a filter (see Figure 9). Under these circumstances there was no significant observable difference between the performances of the two photocatalysts. Indeed, in these tests both catalysts produced almost no dye decolourisation. This result is somewhat surprising as BTO-Fe_2O_3-0.001M demonstrated enhanced absorption in the visible-light range compared with bare BTO (Figure 5). However, this is reasonable considering the low mass ratio of Fe_2O_3 in the heterostructured photocatalyst (0.16% for BTO-Fe_2O_3-0.001M), and the relatively low visible-light absorption for this best-performing catalyst. Therefore, the influence of increased visible-light absorption in BTO-Fe_2O_3-0.001M on its improved performance can be ruled out, and it is $BaTiO_3$ that dominantly generates photoelectrons and holes for BTO-Fe_2O_3-0.001M. In addition, the minor degradation observed under visible light also demonstrated the limited contribution from photosensitization of RhB in

our photocatalytic system. This could be related to the band bending induced by ferroelectric polarization, which hinders the electron transfer from RhB to the conduction band of photocatalysts[31].

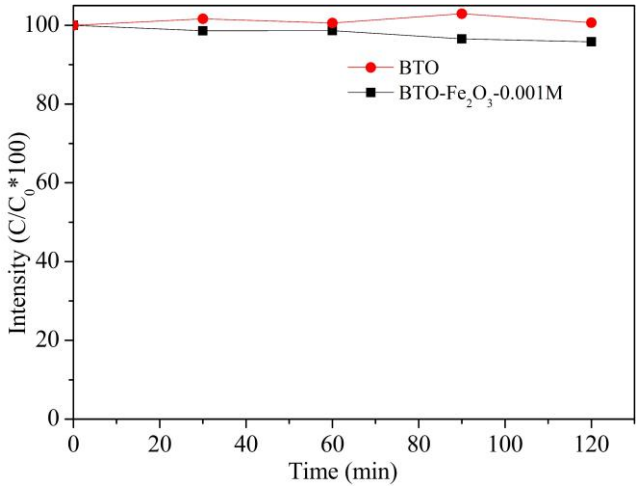

Figure 9. Photodecolourisation profiles of RhB with BTO and BTO-Fe_2O_3-0.001M under visible light. No significant difference is observed, indicating the enhanced visible-light absorption of BTO-Fe_2O_3-0.001M has limited contribution to the improved photoactivity.

The third reason is the band-gap configuration in the composite photocatalysts leading to a local electric field capable of separating photoexcited carriers. We show the relative band positions for $BaTiO_3$ and Fe_2O_3 in Figure 10a. We have determined the band positions for $BaTiO_3$ and α-Fe_2O_3 using the empirical formula, $E_{CB} = X - E^e - 0.5E_g$;[32,33] where X represents the electronegativity of the semiconductor, E^e is the energy of free electrons on the hydrogen scale (about 4.5 eV), and E_g is the band gap energy of the semiconductor. The band gap energy of $BaTiO_3$ and Fe_2O_3 are assumed to be 3.14 eV and 1.88 eV (Fig. 5b). The conduction band edges of $BaTiO_3$ and Fe_2O_3 are calculated to be at -0.83 eV and 0.45 eV versus Normal Hydrogen Electrode (NHE) with the valence band positions at 2.31 eV and 2.33 eV versus NHE. Our band

edge positions are in good agreement with previously reported results.[34,35] The Fermi level position of n-type $BaTiO_3$ is assumed to be at 0.1 eV lower than the conduction band edge.[36,37] The work function for α-Fe_2O_3 5.4 eV situates its Fermi level ca. 0.61 eV below the conduction band edge.[38]

According to the models of a ferroelectric/semiconductor heterostructure proposed by Watanabe,[39,40] the band bending contributed from the polarization of ferroelectrics will counteract or superimpose the band bending due to the heterojunction. This model has been successfully applied in heterostructured ceramic powders composed of ferroelectric (Ba, Sr)TiO_3 core and TiO_2 shells[36,37]. Based on these, band configurations of heterostructured BTO/α-Fe_2O_3 were proposed (Fig. 10b, c).

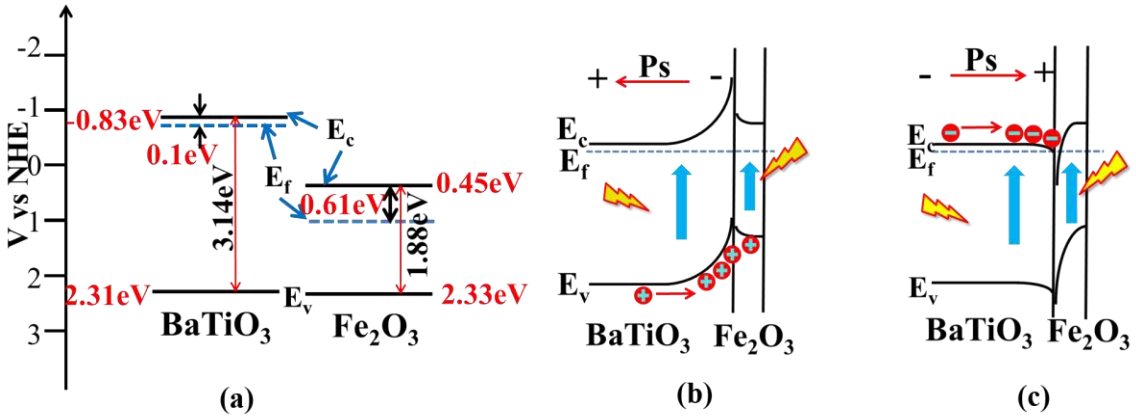

Figure 10. (a) Band positions and Fermi level of independent $BaTiO_3$ and Fe_2O_3, Schematic of band configuration after BTO and Fe_2O_3 coupled together with negative polarization (b) and positive polarization (c) respectively.

As presented in Fig. 10 b, c, with negative (positive) polarization, the holes (electrons) generated in BTO will move towards the interface due to its internal ferroelectric polarization. Holes can easily inject into Fe_2O_3 due to their valence band position differences (Fig. 10b). Photoelectrons

need to overcome the interfacial barrier or tunnel through the Fe_2O_3 layer to be involved in chemical reactions (Fig. 10c). We have calculated the electron tunneling probability using previously reported methods,[41] see Figure S6, and show that the probability of tunneling is negligible. Therefore, it can be speculated that it is necessary for photoelectrons accumulated in the interface to have a direct contact with dye solution species to drive the photodegradation.

Considering the optimum photodegradation activity of BTO-Fe_2O_3-0.001M, where Fe_2O_3 nanoparticles exist in a thin island-like form instead of a complete layer, a typical morphology model was proposed, as presented in Figure 11. The island-like morphology of Fe_2O_3 on the surface of $BaTiO_3$ allows the photons to reach $BaTiO_3$ exciting both Fe_2O_3 and $BaTiO_3$ (Figure 11a). There are numerous triple points between $BaTiO_3$, Fe_2O_3 and dye solutions, where charge carriers accumulate nearby. Meanwhile these triple points allow dye solution to contact with charge carriers directly. Thereafter H_2O, O_2, OH^-, and RhB molecule in dye solution can have a series of reactions with charge carriers, leading to the observed photodegradation (Figure 11b). Therefore, these triple points are critical for redox reactions through providing active sites for both reduction and oxidation. When the loading quantity of Fe_2O_3 is higher, the number of triple points reduced and the continuous Fe_2O_3 layer formed around BTO absorb the majority of irradiation light, suppressing the photoexcitation of BTO (Figure 11c). In addition, the limited contact between dye solutions and electrons/holes in BTO may also account for the deterioration of photocatalytic performance at higher Fe_2O_3 loading.

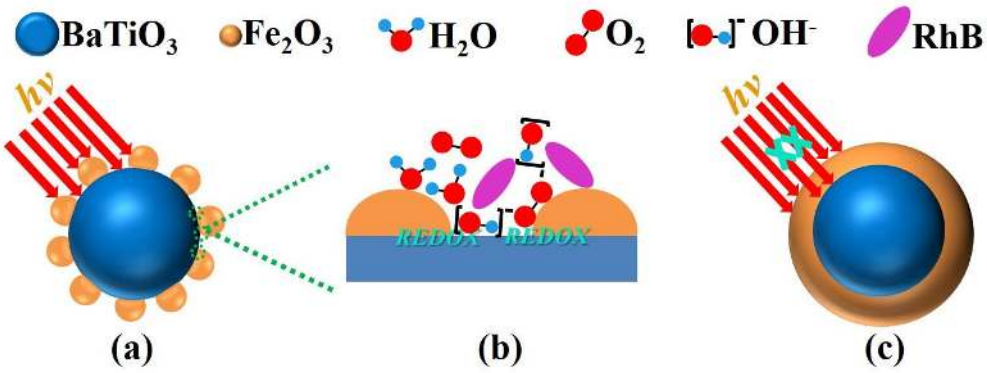

Figure 11. A schematic showing the influence of the existing morphology of Fe_2O_3, (a) the island-like morphology allows the irradiation light to excite $BaTiO_3$ in addition to Fe_2O_3, (b) the triple points between the dye solution, Fe_2O_3 and $BaTiO_3$ provide active sites for REDOX (reduction and oxidation) reactions, (c) the thick layer of Fe_2O_3 may hinder the light to excite $BaTiO_3$.

Based on the discussion above, it can be concluded that the improved charge carrier separation arising from both heterojunction band bending and ferroelectric dipole account for the highest photocatalytic activity of BTO-Fe_2O_3-0.001M. Meanwhile the interface morphology control of Fe_2O_3 on BTO surface is also crucial for the excellent performance.

To further support our claim on the enhanced charge carrier separation, photoluminescence spectrum analysis was carried out to evaluate the charge carrier recombination of photocatalysts and the results are shown in Figure 12a. A stronger PL peak intensity usually implies a higher chance of recombination between electrons and holes.[25,26] As can be seen, after introducing Fe_2O_3, the PL peak intensity of BTO dropped significantly, indicating a higher charge separation efficiency. In addition, the transient photocurrent was measured on a three-electrode electrochemical system when the photocatalyst acting as the working electrode. When the light was turned on, both BTO and BTO-Fe_2O_3-0.001M showed an apparent photocurrent as expected

(Fig. 12b). However, the photocurrent density obtained in BTO-Fe_2O_3-0.001M was about 1.3 times that of BTO, indicating a more effective charge carrier separation in BTO-Fe_2O_3-0.001M. This is consistent with the PL spectra and the trend of observed photocatalytic performance.

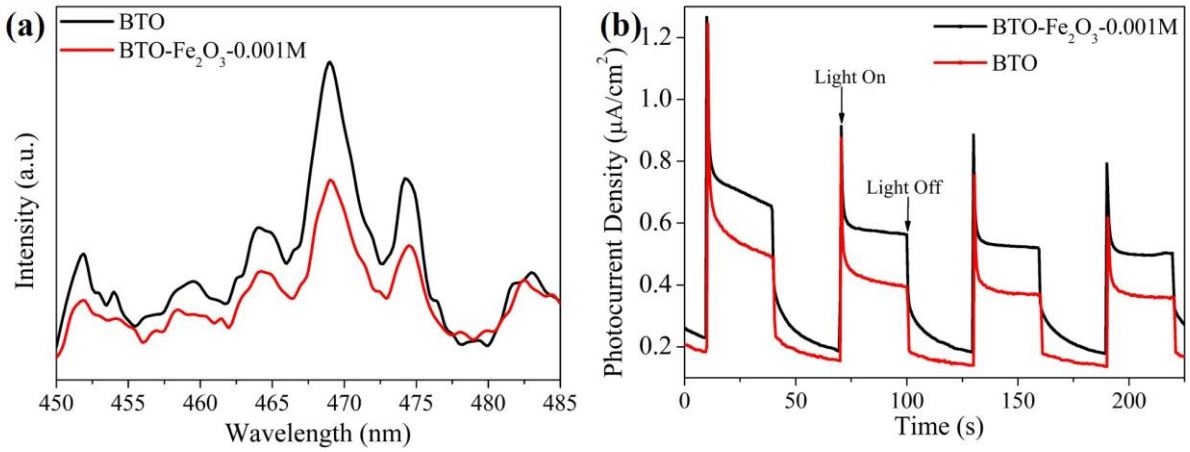

Figure 12. (a) Photoluminescence spectra of BTO and BTO-Fe_2O_3-0.001M. The weaker PL peaks imply a lower recombination chance for BTO-Fe_2O_3-0.001M. (b) Photocurrent density *vs.* time of BTO and BTO-Fe_2O_3-0.001M measured with a voltage of 0.8 V (vs. Ag/AgCl). A much higher photocurrent density was obtained in BTO-Fe_2O_3-0.001M, indicating a more effective charge carrier separation.

Last but not least, the external screening of the surface polarization charge in BTO will induce holes and electrons in Fe_2O_3 to migrate in opposite directions and then the drawbacks of short charge carrier lifetime of Fe_2O_3 will be overcame. Although the contributions from the charge carriers of Fe_2O_3 to the overall photocatalytic performance is limited (Fig. 9) due to its very low amount, one can still expect to steer charge carrier motion of a semiconductor and improve photocatalytic performance based on ferroelectric dipoles considering the external screening of ferroelectric surface charge. The similar statement that the built-in electric field of $BaTiO_3$ nanocrystals can assist in separating the photo-induced charge carriers of surface-attached Ag_2O

also supports our hypothesis[42]. This speculation can be further supported by the conclusions that the piezoelectric polarization of ZnO nanorods was verified to be capable to reduce charge carrier recombination and extend lifetime in a polymer/ZnO photovoltaic devices[43]. In addition, the non-ferroelectric cubic BTO instead of ferroelectric tetragonal BTO was also employed as a substrate to combine with α-Fe_2O_3 to investigate the effect of ferroelectric dipole. The comparison of photodegradation profiles between the ferroelectric and non-ferroelectric based composited photocatalysts is shown in Fig. S7. Under the same preparation method, ferroelectric BTO/α-Fe_2O_3 showed a higher photodegradation efficiency than non-ferroelectric BTO/α-Fe_2O_3. This priority should be related to the ferroelectric polarization of BTO as well. As BTO is the dominate component generating charge carriers in the heterostructured photocatalysts, the built-in electric field in ferroelectric BTO assists charge carriers separation and more electrons/holes can involve in the following degradation.

Conclusion

$BaTiO_3$/α-Fe_2O_3 photocatalysts with different mass ratios of Fe_2O_3 were produced. The optimum photocatalytic activity was obtained for $BaTiO_3$-Fe_2O_3-0.001M with an enhanced photodecolourisation rate of RhB dye when compared to control systems of pure $BaTiO_3$ and Fe_2O_3. The improved performance was attributed to efficient charge carrier separation in the interface due to heterojunction band alignment and ferroelectric polarization. We also show that a triple point between $BaTiO_3$, α-Fe_2O_3 and dye solution is important to enable the required redox reactions to proceed. The catalysts demonstrate good photocatalytic stability in a recycling test and holes were verified as the dominant reactive species during the photodegradation. We propose that the junction between a ferroelectric substrate and semiconductor photocatalyst provides a new strategy to manipulate charge transport and enhance performance.

Supporting Information.

SEM micrographs of bare BTO, Comparison of the XPS spectra between BTO and BTO-Fe_2O_3-0.001M (Ba 3d, Ti 2p and O 1s), TEM micrographs of bare BTO, BTO-Fe_2O_3-0.1M, BTO-Fe_2O_3-0.5M and Fe_2O_3, Linear fitted function relationship of C_0-C_t versus t, BET surface areas of powders used in this study and the adsorption of RhB dye molecules, The calculated reaction rates of different photocatalysts scaled by surface area, Schematic showing the model adopted to calculate the probability for one electron in BTO to tunnel through α-Fe_2O_3 layer, Comparison of photodegradation profiles using ferroelectric BTO/α-Fe_2O_3 and non-ferroelectric BTO/α-Fe_2O_3. This material is available free of charge via the Internet at http://pubs.acs.org.

AUTHOR INFORMATION

Corresponding Author

* s.c.dunn@qmul.ac.uk

Author Contributions

The manuscript was written through contributions of all authors. All authors have given approval to the final version of the manuscript.

ACKNOWLEDGMENT

This work was financially supported by the National Nature Science Foundation of China (No. 51602185), China Postdoctoral Science Foundation (2017M613038), and Doctoral Scientific Research Startup Foundation of Shaanxi University of Science and Technology (No. 2016BJ-09). Dr. Xingang Kong is acknowledged for his assisting in the photoelectrochemical test.

REFERENCES

(1) Mills, A.; Davies, R. H.; Worsley, D. Water Purification by Semiconductor Photocatalysis. *Chem. Soc. Rev.* **1993**, *22*, 417–425.

(2) Di Paola, A.; García-López, E.; Marcì, G.; Palmisano, L. A Survey of Photocatalytic Materials for Environmental Remediation. *J. Hazard. Mater.* **2012**, *211–212*, 3–29.

(3) Qu, Y.; Duan, X. Progress, Challenge and Perspective of Heterogeneous Photocatalysts. *Chem. Soc. Rev.* **2013**, *42*, 2568–2580.

(4) Tong, H.; Ouyang, S.; Bi, Y.; Umezawa, N.; Oshikiri, M.; Ye, J. Nano-Photocatalytic Materials: Possibilities and Challenges. *Adv. Mater.* **2012**, *24*, 229–251.

(5) Kim, H. G.; Borse, P. H.; Jang, J. S.; Jeong, E. D.; Jung, O.-S.; Suh, Y. J.; Lee, J. S. Fabrication of $CaFe_2O_4/MgFe_2O_4$ Bulk Heterojunction for Enhanced Visible Light Photocatalysis. *Chem. Commun.* **2009**, 39, 5889–5891.

(6) Baker, D. R.; Kamat, P. V. Photosensitization of TiO_2 Nanostructures with CdS Quantum Dots: Particulate versus Tubular Support Architectures. *Adv. Funct. Mater.* **2009**, *19*, 805–811.

(7) Wang, C.; Thompson, R. L.; Ohodnicki, P.; Baltrus, J.; Matranga, C. Size-Dependent Photocatalytic Reduction of CO_2 with PbS Quantum Dot Sensitized TiO_2 Heterostructured Photocatalysts. *J. Mater. Chem.* **2011**, *21*, 13452–13457.

(8) Chen, X.; Shen, S.; Guo, L.; Mao, S. S. Semiconductor-Based Photocatalytic Hydrogen Generation. *Chem. Rev.* **2010**, *110*, 6503–6570.

(9) Moniz, S. J. A.; Shevlin, S. A.; Martin, D. J.; Guo, Z.-X.; Tang, J. Visible-Light Driven Heterojunction Photocatalysts for Water Splitting - a Critical Review. *Energy Environ. Sci.* **2015**, *8*, 731–759.

(10) Tiwari, D.; Dunn, S. Photochemistry on a Polarisable Semi-Conductor: What Do We Understand Today? *J. Mater. Sci.* **2009**, *44*, 5063–5079.

(11) Liu, F.; Fina, I.; Gutiérrez, D.; Radaelli, G.; Bertacco, R.; Fontcuberta, J. Selecting Steady and Transient Photocurrent Response in $BaTiO_3$ Films. *Adv. Electron. Mater.* **2015**, *1*, 1500171.

(12) Kholkin, A.; Boiarkine, O.; Setter, N. Transient Photocurrents in Lead Zirconate Titanate Thin Films. *Appl. Phys. Lett.* **1998**, *72*, 130–132.

(13) Morris, M. R.; Pendlebury, S. R.; Hong, J.; Dunn, S.; Durrant, J. R. Effect of Internal Electric Fields on Charge Carrier Dynamics in a Ferroelectric Material for Solar Energy Conversion. *Adv. Mater.* **2016**, *28*, 7123–7128.

(14) Stock, M.; Dunn, S. $LiNbO_3$—A Polar Material for Solid-Gas Artificial Photosynthesis. *Ferroelectrics* **2011**, *419*, 9–13.

(15) Cui, Y.; Briscoe, J.; Dunn, S. Effect of Ferroelectricity on Solar-Light-Driven Photocatalytic Activity of $BaTiO_3$—Influence on the Carrier Separation and Stern Layer Formation. *Chem. Mater.* **2013**, *25*, 4215–4223.

(16) Inoue, Y.; Okamura, M.; Sato, K. A Thin-Film Semiconducting Titanium Dioxide Combined with Ferroelectrics for Photoassisted Water Decomposition. *J. Phys. Chem.* **1985**, *89*, 5184–5187.

(17) Burbure, N. V; Salvador, P. A.; Rohrer, G. S. Photochemical Reactivity of Titania Films on $BaTiO_3$ Substrates: Origin of Spatial Selectivity. *Chem. Mater.* **2010**, *22*, 5823–5830.

(18) Zhu, A.; Zhao, Q.; Li, X.; Shi, Y. $BiFeO_3/TiO_2$ Nanotube Arrays Composite Electrode: Construction, Characterization, and Enhanced Photoelectrochemical Properties. *ACS Appl. Mater. Interfaces* **2013**, *6*, 671–679.

(19) Li, S.; Lin, Y.-H.; Zhang, B.-P.; Li, J.-F.; Nan, C.-W. $BiFeO_3/TiO_2$ Core-Shell Structured Nanocomposites as Visible-Active Photocatalysts and Their Optical Response Mechanism. *J. Appl. Phys.* **2009**, *105*, 54310.

(20) Huang, H.; Li, D.; Lin, Q.; Shao, Y.; Chen, W.; Hu, Y.; Chen, Y.; Fu, X. Efficient Photocatalytic Activity of PZT/TiO_2 Heterojunction under Visible Light Irradiation. *J. Phys. Chem. C* **2009**, *113*, 14264–14269.

(21) Li, L.; Zhang, Y.; Schultz, A. M.; Liu, X.; Salvador, P. a.; Rohrer, G. S. Visible Light Photochemical Activity of Heterostructured $PbTiO_3$–TiO_2 Core–shell Particles. *Catal. Sci. Technol.* **2012**, *2*, 1945.

(22) Sivula, K.; Le Formal, F.; Grätzel, M. Solar Water Splitting: Progress Using Hematite (α-Fe_2O_3) Photoelectrodes. *ChemSusChem* **2011**, *4*, 432–449.

(23) Wheeler, D. A.; Wang, G.; Ling, Y.; Li, Y.; Zhang, J. Z. Nanostructured Hematite: Synthesis, Characterization,charge Carrier Dynamics, and Photoelectrochemical Properties. *Energy Environ. Sci.* **2012**, *5*, 6682–6702.

(24) Wang, G.; Ling, Y.; Wheeler, D. A.; George, K. E. N.; Horsley, K.; Heske, C.; Zhang, J. Z.; Li, Y. Facile Synthesis of Highly Photoactive α-Fe_2O_3-Based Films for Water Oxidation. *Nano Lett.* **2011**, *11*, 3503–3509.

(25) Moniz, S. J. A.; Shevlin, S. A.; An, X.; Guo, Z.-X.; Tang, J. Fe_2O_3–TiO_2 Nanocomposites for Enhanced Charge Separation and Photocatalytic Activity. *Chem. – Eur. J.* **2014**, *20*, 15571–15579.

(26) Guo, Y.; Zhang, G.; Liu, J.; Zhang, Y. Hierarchically Structured α-Fe_2O_3/Bi_2WO_6 Composite for Photocatalytic Degradation of Organic Contaminants under Visible Light Irradiation. *RSC Adv.* **2013**, *3*, 2963–2970.

(27) Yamashita, T.; Hayes, P. Analysis of XPS Spectra of Fe^{2+} and Fe^{3+} Ions in Oxide Materials. *Appl. Surf. Sci.* **2008**, *254*, 2441–2449.

(28) Chang, J.-C.; Tsai, W.-J.; Chiu, T.-C.; Liu, C.-W.; Chao, J.-H.; Lin, C.-H. Chemistry in a Confined Space: Characterization of Nitrogen-Doped Titanium Oxide Nanotubes Produced by Calcining Ammonium Trititanate Nanotubes. *J. Mater. Chem.* **2011**, *21*, 4605–4614.

(29) Sun, S.-P.; Li, C.-J.; Sun, J.-H.; Shi, S.-H.; Fan, M.-H.; Zhou, Q. Decolorization of an Azo Dye Orange G in Aqueous Solution by Fenton Oxidation Process: Effect of System Parameters and Kinetic Study. *J. Hazard. Mater.* **2009**, *161*, 1052–1057.

(30) Naresh, G.; Mandal, T. K. Excellent Sun-Light-Driven Photocatalytic Activity by Aurivillius Layered Perovskites, $Bi_{5-x}La_xTi_3FeO_{15}$ (x=1,2). *ACS Appl. Mater. Interfaces* **2014**, *15*, 21000–21010.

(31) Cui, Y.; Goldup, S. M.; Dunn, S. Photodegradation of Rhodamine B over Ag Modified Ferroelectric $BaTiO_3$ under Simulated Solar Light: Pathways and Mechanism. *RSC Adv.* **2015**, *5*, 30372–30379.

(32) Butler, M. A.; Ginley, D. S. Prediction of Flatband Potentials at Semiconductor-Electrolyte Interfaces from Atomic Electronegativities. *J. Electrochem. Soc.* **1978**, *125*, 228–232.

(33) Kim, Y. Il; Atherton, S. J.; Brigham, E. S.; Mallouk, T. E. Sensitized Layered Metal Oxide Semiconductor Particles for Photochemical Hydrogen Evolution from Nonsacrificial Electron Donors. *J. Phys. Chem.* **1993**, *97*, 11802–11810.

(34) Hou, Y.; Zuo, F.; Dagg, A.; Feng, P. Visible Light-Driven α-Fe_2O_3 Nanorod/Graphene/$BiV_{1-x}Mo_xO_4$ Core/Shell Heterojunction Array for Efficient Photoelectrochemical Water Splitting. *Nano Lett.* **2012**, *12*, 6464–6473.

(35) Lin, X.; Xing, J.; Wang, W.; Shan, Z.; Xu, F.; Huang, F. Photocatalytic Activities of Heterojunction Semiconductors Bi_2O_3/$BaTiO_3$: A Strategy for the Design of Efficient Combined Photocatalysts. *J. Phys. Chem. C* **2007**, *111*, 18288–18293.

(36) Li, L.; Liu, X.; Zhang, Y.; Salvador, P. A.; Rohrer, G. S. Heterostructured (Ba,Sr)TiO_3/TiO_2 Core/shell Photocatalysts: Influence of Processing and Structure on Hydrogen Production. *Int. J. Hydrogen Energy* **2013**, *38*, 6948–6959.

(37) Li, L.; Rohrer, G. S.; Salvador, P. A. Heterostructured Ceramic Powders for Photocatalytic Hydrogen Production: Nanostructured TiO_2 Shells Surrounding Microcrystalline (Ba,Sr)TiO_3 Cores. *J. Am. Ceram. Soc.* **2012**, *95*, 1414–1420.

(38) Fan, Z.; Wen, X.; Yang, S.; Lu, J. G. Controlled P- and N-Type Doping of Fe_2O_3 Nanobelt Field Effect Transistors. *Appl. Phys. Lett.* **2005**, *87*, 13113.

(39) Watanabe, Y. Electrical Transport through Pb(Zr,Ti)O_3 P-N and P-P Heterostructures Modulated by Bound Charges at a Ferroelectric Surface: Ferroelectric P-N Diode. *Phys. Rev. B* **1999**, *59*, 11257–11266.

(40) Watanabe, Y. Energy Band Diagram of Ferroelectric Heterostructures and Its Application to the Thermodynamic Feasibility of Ferroelectric FET. *Solid State Ionics* **1998**, *108*, 59–65.

(41) Loh, L.; Briscoe, J.; Dunn, S. Enhanced Performance with Bismuth Ferrite Perovskite in ZnO Nanorod Solid State Solar Cells. *Nanoscale* **2014**, *6*, 7072–7078.

(42) Li, H.; Sang, Y.; Chang, S.; Huang, X.; Zhang, Y.; Yang, R.; Jiang, H.; Liu, H.; Wang, Z. L. Enhanced Ferroelectric-Nanocrystal-Based Hybrid Photocatalysis by Ultrasonic-Wave-Generated Piezophototronic Effect. *Nano Lett.* **2015**, *15*, 2372–2379.

(43) Shoaee, S.; Briscoe, J.; Durrant, J. R.; Dunn, S. Acoustic Enhancement of Polymer/ZnO Nanorod Photovoltaic Device Performance. *Adv. Mater.* **2014**, *26*, 263–268.

Table of Content